JACS
JOURNAL OF THE AMERICAN CHEMICAL SOCIETY

pubs.acs.org/JACS

Article

Triple-Wavelength Lasing with a Stabilized β-$LaBSiO_5$:Nd^{3+} Crystal

Lingyun Li,*,# Fazheng Huang,# Yi Shi,# Zhong-Zhen Luo, Guo-Qiang Wang, Xin-Xiong Li, Bingxuan Li, Lizhen Zhang, Yi Yu, Ya-Nan Feng, Chengkai Yang, Yan Yu,* and Kenneth R. Poeppelmeier*

Cite This: J. Am. Chem. Soc. 2022, 144, 11822−11830

Read Online

ACCESS | Metrics & More | Article Recommendations | Supporting Information

ABSTRACT: Multi-wavelength lasers, especially the triple-wavelength laser around 1060 nm, could be produced by the $^4F_{3/2} \rightarrow {}^4I_{11/2}$ transition of Nd^{3+} and present numerous challenges and opportunities in the field of optoelectronics. The Nd^{3+}-doped high-temperature phase of $LaBSiO_5$ (β-LBSO) is an ideal crystal to produce triple-wavelength lasers; however, the crystal growth is challenging because of the phase transition from β-LBSO to low-temperature phase (α-LBSO) at 162 °C. This phase transition is successfully suppressed when the doping content of Nd^{3+} is larger than 6.3 at. %, and the Nd^{3+}-doped β-LBSO is stable at room temperature. The local disorder of BO_4 tetrahedra due to Nd^{3+} doping is essential to the stabilization of β-LBSO. For the first time, the β-LBSO:8%Nd^{3+} crystal with a dimension of 1.8 × 1.8 × 1.8 cm^3 is obtained through the top-seeded solution method. The crystal shows strong optical absorption in the range of 785−815 nm, matching well with the commercial laser diode pumping source. The optical emission of $^4F_{3/2} \rightarrow {}^4I_{11/2}$ splits into four peaks with the highest optical emission cross section of 2.14×10^{-20} cm^2 at 1068 nm. The continuous-wave triple-wavelength generation of coherent light at 1047, 1071, and 1092 nm is achieved with the highest output power of 235 mW and efficiency of 12.1%.

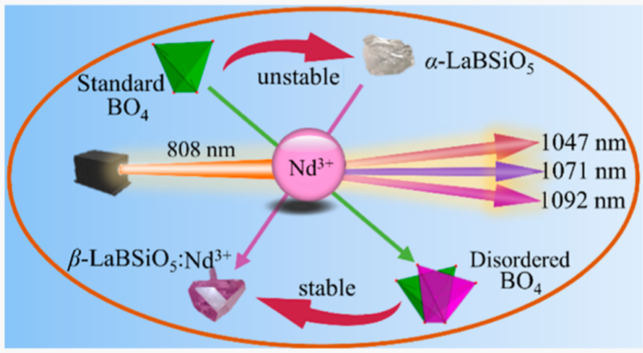

■ INTRODUCTION

Multi-wavelength lasers with simultaneous emissions of two or more lasers in one beam have great applications in the field of tera hertz (THz),[1] precision metrology,[2] holography,[3] medical treatment,[4] and laser interferometry.[5] Most of the multi-wavelength lasers are produced by Nd^{3+}-doped crystals, such as Nd^{3+}-doped yttrium aluminum garnet (YAG:Nd^{3+}),[6] yttrium vanadate (YVO_4:Nd^{3+}),[7] gadolinium vanadate ($GdVO_4$:Nd^{3+}),[8] and yttrium-aluminate (YAP:Nd^{3+}) crystals[9] since the optical emission of Nd^{3+} corresponding to the $^4F_{3/2} \rightarrow {}^4I_{11/2}$ transition can split into several peaks around 1064 nm according to the Stark sublevels of $^4I_{11/2}$. For example, Cho et al. reported the simultaneous laser emissions at 1047 and 1053 nm using a Nd^{3+}-doped lithium yttrium fluoride (YLF:Nd^{3+}) crystal as gain media at the cryogenic temperature.[10] An orthogonally polarized dual-wavelength laser working at 1052 and 1081 nm was also obtained based on the $LaMgB_5O_{10}$:Nd^{3+} crystal, which was diode-pumped with a continuous-wave (CW) way mode.[11] A dual-wavelength laser at 1068 and 1074 nm was realized on the $LaBO_2MoO_4$:Nd^{3+} crystal.[12] However, most multi-wavelength lasers around 1064 nm work in a dual-wavelength mode,[6,10−13] as listed in Table S1. It would have significant practical potential if an Nd^{3+}-doped crystal could produce triple-wavelength lasers based on the $^4F_{3/2} \rightarrow {}^4I_{11/2}$ transition. For example, a dual-wavelength laser can produce only one THz wave based on the differential frequency technology, but a triple-wavelength laser can produce three, which greatly expands the THz light source. However, the main obstacle to developing a triple-wavelength laser is the lack of suitable laser crystals.

The high-temperature phase of $LaBSiO_5$ (β-LBSO) with the advantage of functional borate and silicate groups would be an ideal host crystal for Nd^{3+} ions to obtain a triple-wavelength laser. β-LBSO was first discovered as a mineral in northwestern Queensland in 1955.[14] It crystallizes in the $P3_121$ space group with cell parameters $a = b = 6.827(2)$ (Å), $c = 6.779(2)$ (Å), $V = 273.63$ (Å^3), and $Z = 3$.[15] β-LBSO is stable above 162 °C and transforms to the low-temperature phase of α-LBSO below 162 °C. α-LBSO crystallizes in the trigonal system with space group of $P3_1$ and cell parameters $a = b = 6.874(1)$ (Å), $c = 6.717(3)$ (Å), $V = 274.87$ (Å^3), and $Z = 3$ (Figure S1).[16] The growth of β-LBSO single crystals has drawn attention since its discovery. Leonyuk et al. attempted to grow the crystal through a flux method by using $K_2Mo_3O_{10}$ and KF as the solvent. Crystals of up to 3 mm were obtained when the flux cooled down from 1140 °C.[17] Sha et al. also reported crystals from a

Received: April 22, 2022
Published: June 9, 2022

https://doi.org/10.1021/jacs.2c04331
J. Am. Chem. Soc. 2022, 144, 11822−11830

flux containing Li_2MoO_4 during the temperature range of 950−750 °C.[18] The authors obtained a transparent crystal plate with the dimension of 4 × 4 mm^2 by a spontaneous nucleation method. However, the above crystals were α-LBSO. Our previous study indicated that a large crystal with the dimension of 1.2 × 1.0 × 0.8 cm^3 can be obtained through a top-seeded solution method (TSSG) during the temperature range of 1039−750 °C by using a flux composed by $LaBO_3$, SiO_2, and Li_2MoO_4.[19] Unfortunately, the obtained crystal also transformed to be α-LBSO and fractured at room temperature because of the stress release during the phase transition (Figure S2). To date, the successful growth of β-LBSO single crystals has yet to be achieved.

The challenge is two-fold, first is controlling or eliminating the phase transition of β-LBSO on cooling to room temperature and the second is growing large β-LBSO single crystals. The strategies such as strain adjustment,[20] grain size control,[21] annealing process,[22] and doping[23] are commonly used to manipulate the phase composition or phase transition of functional materials such as VO_2, TiO_2, and ZrO_2.[24] The metal−insulator transition (MIT) temperature of the VO_2 film could be lowered from 68 to 31 °C by adjusting the strain/stress between the film and the substrate.[25] Doping of La^{3+}, Co^{2+}, and Fe^{3+} ions can promote TiO_2 transformation from the anatase phase to the rutile phase,[26] while Al^{3+} and Tb^{3+} doping restrain the phase transition between them.[27] Meanwhile, one can make the high-temperature cubic phase ZrO_2 stable even at room temperature by doping Sc^{3+} ions or controlling the grain size at the nanometer level. The tuning of phase transitions in the above materials is related to modification of the lattice energy and the appearance of the intermediate phase.[24] However, for the β-LBSO single crystal, strain adjustment and grain size regulation are not applicable to eliminate the phase transition. On the contrary, β-LBSO exhibits excellent doping capability with rare-earth ions such as Ce^{3+}, Tb^{3+}, Eu^{3+}, Pr^{3+}, and Sm^{3+},[28] which display excellent photoluminescence properties.[29] As a widely used method to tune the phase transition of functional materials, doping is a promising route to eliminate the phase transition of β-LBSO crystal and to stabilize it to room temperature.

In this work, the phase tuning of β-LBSO via Nd^{3+} doping was studied. The phase transition of β-LBSO crystal can be suppressed with the doping ratio of Nd^{3+} above 6.3% (mol). The introduction of Nd^{3+} into β-LBSO renders the O3 atom statistically distributing and the BO_4 polyhedra disordered, which is crucial for the stabilization of β-LBSO at room temperature. We obtained a large β-LBSO:8%Nd^{3+} crystal for the first time through the TSSG method. The Nd^{3+} ions in this crystal are both optically active centers and a structure stabilization agent. The β-LBSO:8%Nd^{3+} crystal shows strong optical absorption in the range of 785−815 nm, matching well with the commercial laser diode (LD) pumping source. The optical emission of ${}^4F_{3/2} \rightarrow {}^4I_{11/2}$ splits into four peaks with the highest optical emission cross section of 2.14 × 10^{-20} cm^2 at 1068 nm. Most importantly, a triple-wavelength CW laser with 1047, 1071, and 1092 nm in one coherent laser beam was achieved. This laser beam displays the largest wavelength difference of the triple-wavelength lasers and the highest output laser power of 235 mW with 808 nm LD as the pumping source.

■ RESULTS AND DISCUSSION

Influence of Nd^{3+} Doping on the Phase Transition of β-LBSO and Crystal Growth of Nd^{3+}-Doped β-LBSO. The Nd^{3+} doping can suppress the phase transition of β-LBSO. The evolution of the enthalpy of the phase transition and the transition temperature of the Nd^{3+}-doped samples grown by the spontaneous nucleation method (Figures S3 and S4) versus doping rate are shown in Figure 1a. As displayed, the

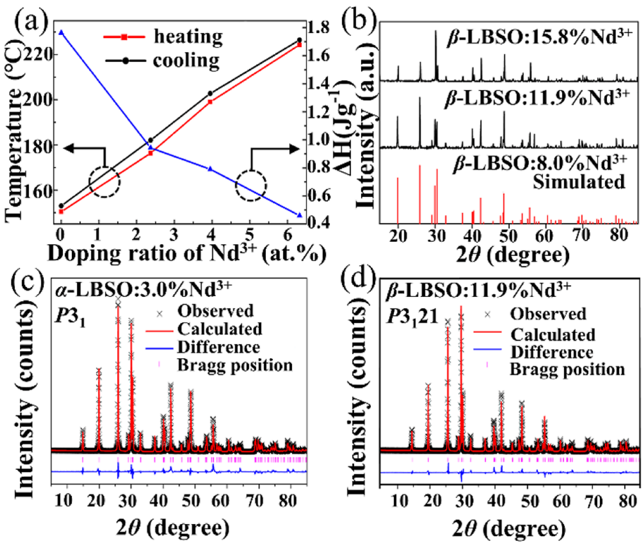

Figure 1. Phase-transition temperature, enthalpy changes of LBSO:x%Nd^{3+} (a); PXRD patterns of β-LBSO:11.9%Nd^{3+} and β-LBSO:15.8%Nd^{3+} crystals that measured at 22 °C (b); Rietveld refinement results of α-LBSO:3.0%Nd^{3+} with R_{wp} = 9.86%, R_p = 7.38%, and χ^2 = 0.87 (c); and β-LBSO:11.9%Nd^{3+} with R_{wp} = 12.81%, R_p = 9.16%, and χ^2 = 1.60 (d).

phase-transition temperature rises when the doping content increases, indicating that the transition from β-LBSO to α-LBSO becomes more difficult when Nd^{3+} replaces La^{3+}. On the other hand, the transition enthalpy decreases with the increase in Nd^{3+} content. As shown in Figure S5, all β-LBSO samples doped by Nd^{3+} with content no more than 6.3% (mol) have an endothermic peak on the heating curve and an exothermic peak on the cooling curve, indicating a reversible first-order phase transition between α- and β-LBSO. Furthermore, the endothermic and exothermic peaks have disappeared with Nd^{3+} above 6.3%, indicating the elimination of phase transition. To demonstrate the elimination of phase transition, the crystal structure of β-LBSO:8.0%Nd^{3+} at −98 °C was solved. The crystallographic parameters are shown in Tables S2−S4. It crystallizes in the trigonal system and has the same space group $P3_121$ as β-LBSO. Meanwhile, the unit cells of β-LBSO:8.0%Nd^{3+} expand slightly along both the a and b axes compared with that of the undoped β-LBSO. The thermal analysis and single-crystal structural data reveal that the β-LBSO:8.0%Nd^{3+} crystal is stable down to a temperature of −98 °C. As shown in Figure 1b, the powder X-ray diffraction (PXRD) patterns of β-LBSO:11.9%Nd^{3+} and β-LBSO:15.8% Nd^{3+} match well with the simulated pattern of β-LBSO:8.0% Nd^{3+}. Furthermore, the stabilization effect of Nd^{3+} doping was confirmed by the Rietveld fitting of the PXRD data of α-LBSO:3.0%Nd^{3+} and β-LBSO:11.9%Nd^{3+} crystals, as shown in Figure 1c,d. The data of β-LBSO:11.9%Nd^{3+} was refined well with the crystal structure of β-LBSO:8.0%Nd^{3+} as the starting

https://doi.org/10.1021/jacs.2c04331
J. Am. Chem. Soc. 2022, 144, 11822−11830

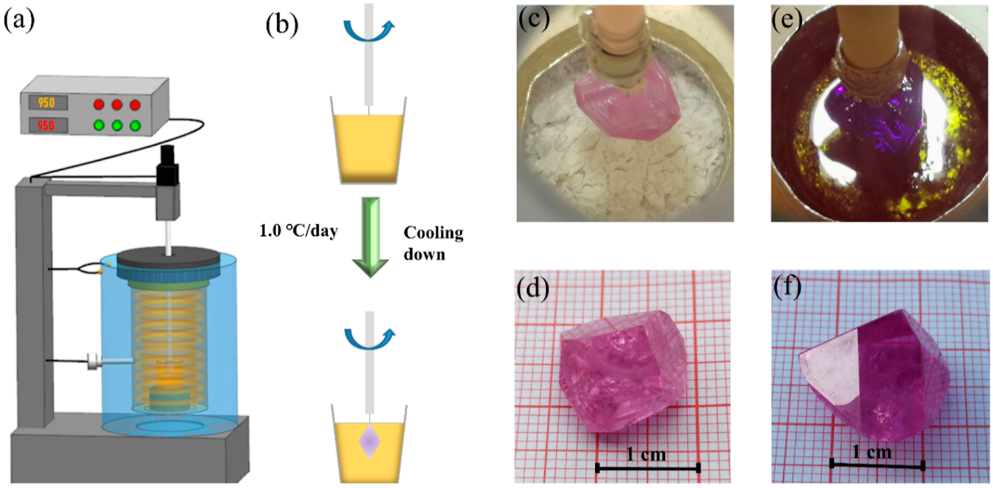

Figure 2. Sketch of TSSG equipment (a) and crystal growth procedure (b). Photos of β-LBSO:8.0%Nd^{3+} crystals (c,d) and β-LBSO:15.8%Nd^{3+} crystals (e,f) that were taken under annealing (c,e) and taken after annealing (d,f). The crystals were grown along the *c* axis from the $LaBO_3$−Li_2MoO_4−SiO_2−B_2O_3 molten system and the photos of (d,f) were taken at 22 °C.

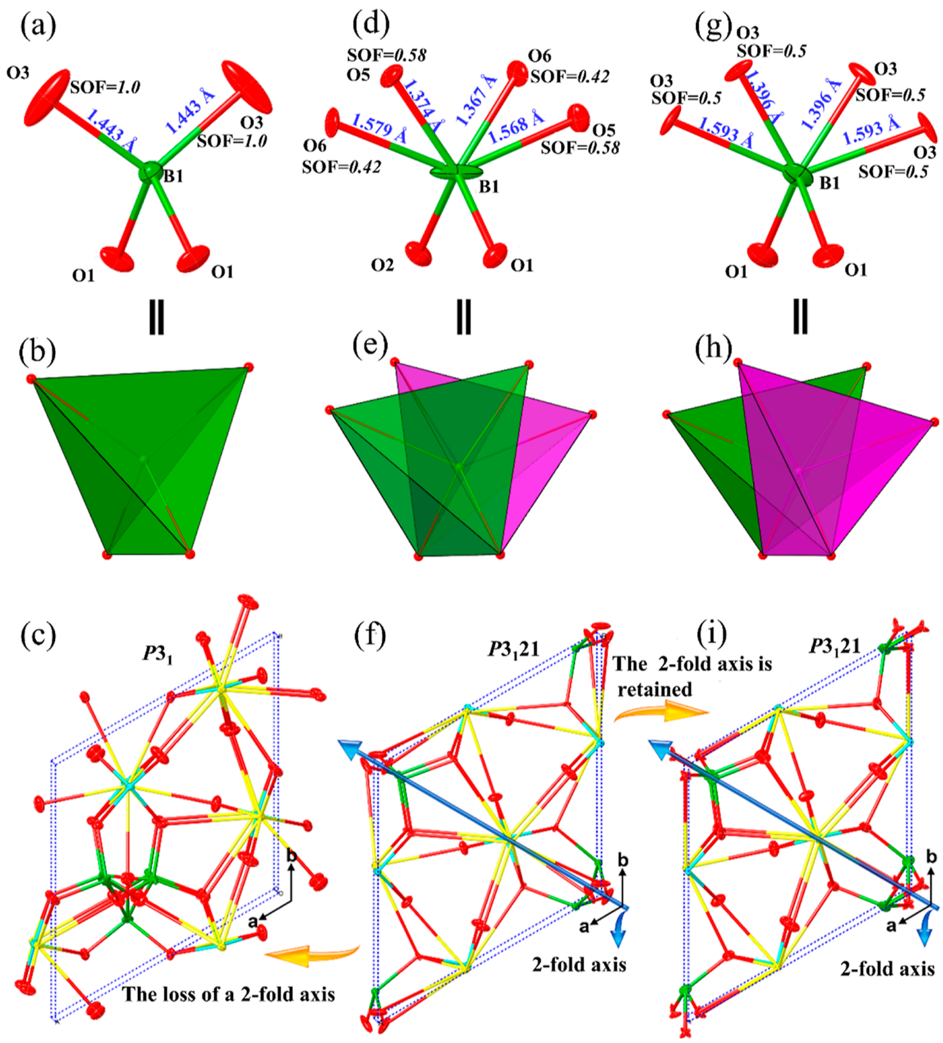

Figure 3. Ball−stick and polyhedral representation of the BO_4 tetrahedra in β-LBSO that crystallized in the $P3_121$ space group (a,b), α-LBSO that crystallized in the $P3_1$ space group (d,e), and β-LBSO:8.0%Nd^{3+} that crystallized in the $P3_121$ space group (g,h). Unit cells of α-LBSO (c), β-LBSO (f), and β-LBSO:8.0%Nd^{3+} (i). BO_4 polyhedra in (e,h) are shown in different colors for clarity. Atomic color code: oxygen, red; silicon, cyan; lanthanide, yellow; and boron, green.

https://doi.org/10.1021/jacs.2c04331
J. Am. Chem. Soc. 2022, 144, 11822−11830

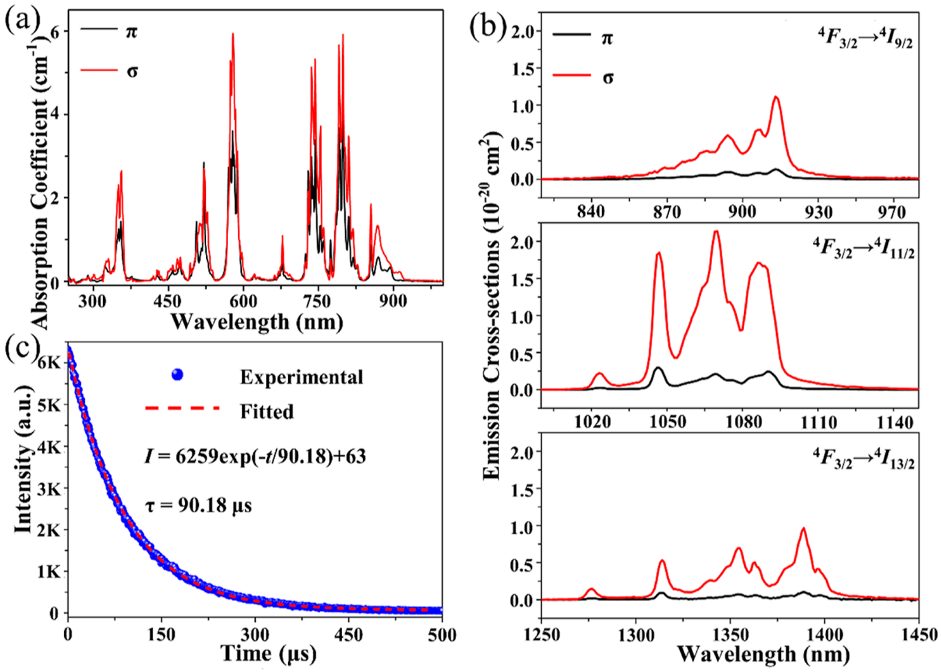

Figure 4. Polarized optical absorption and emission spectra (a,b) and luminescence decay curve of the β-LBSO:8.0%Nd^{3+} crystal (c).

model, indicating that β-LBSO:11.9%Nd^{3+} belongs to the high-temperature phase with space group $P3_121$. Meanwhile, the PXRD pattern of α-LBSO:3.0%Nd^{3+} was fitted well according to the structure of α-LBSO. The stabilization of β-LBSO at room temperature is fundamental to large size crystal growth. The β-LBSO:8.0%Nd^{3+} crystal with a dimension of 1.8 × 1.8 × 1.8 cm^3 and the β-LBSO:15.8%Nd^{3+} crystal with the dimension of 2.3 × 2.3 × 2 cm^3 were successfully grown by the TSSG method from the $LaBO_3$−Li_2MoO_4−SiO_2−B_2O_3 molten system (Figure 2a,b). A c axis seed crystal was used during the growth procedure (Figure S6). Figure 2c−f displays the β-LBSO:8.0%Nd^{3+} and β-LBSO:15.8%Nd^{3+} crystals under and after annealing. The exposed natural planes such as (011), $(1\bar{1}1)$, and $(\bar{1}01)$ form the morphology of these crystals. The phase consistency between the obtained crystals and the resolved structure of β-LBSO:8.0%Nd^{3+} was confirmed by the PXRD patterns presented in Figure S7.

Phase Stabilization Mechanism of Nd^{3+} Doping on β-LBSO. Benefitting from the single-crystal structure data of β-LBSO:8.0%Nd^{3+}, the influence of Nd^{3+} doping on the crystal structure of β-LBSO and the stabilization mechanism was investigated from a crystallographic viewpoint. As reported by Leonyuk and Huang, β-LBSO and α-LBSO crystallize in the $P3_121$ and $P3_1$ space groups, respectively.[16] A detailed structural comparison between them indicates that the most obvious structural variation during the phase transformation is the distortion of the BO_4 tetrahedron. The basic structural units of both structures are identical except that the two oxygen atoms of the BO_4 tetrahedron in α-LBSO split into four oxygen atoms (Figure S8). In β-LBSO that crystallized in the $P3_121$ space group, the atomic displacement parameters of the two oxygen atoms (O3) of the BO_4 tetrahedron are much larger than the other two oxygen atoms (O1) (Tables S5−S7), indicating that the two O3 atoms have a potential position statistical distribution (Figure 3a,b). While in the α-LBSO that crystallized in the $P3_1$ space group, the two O3 atoms split into four positions (O5 and O6) with site occupancy factors of 0.42 and 0.58 (Figure 3d,e). Furthermore, the B−O bond distances vary from 1.443 Å in β-LBSO to 1.374, 1.367, 1.568, and 1.579 Å in α-LBSO during the phase transformation. Such a phase-transformation-induced structural variation can be understood as the regular BO_4 tetrahedron in β-LBSO transforms to two slightly distorted BO_4 tetrahedra with unequal site occupancy as the temperature decreases (Figure 3a,b,d,e). It is noteworthy that such an asymmetric split of the O3 atom results in the loss of the 2-fold rotation axis of the $P3_121$ space group (Figure 3c,f). Consequently, α-LBSO has to crystallize in the $P3_1$ space group. Generally, the skeleton tension of a structure increases as the temperature drops because the thermal vibration of atoms is reduced accordingly. The phase transformation from $P3_121$ to $P3_1$ reveals that the distortion and statistical distribution of the BO_4 tetrahedra may be suppressed at high temperatures due to the weak skeleton tension, and those of the BO_4 tetrahedra become greater to reduce the strong skeleton tension at low temperature. Thus, it can be concluded that a local disorder of a structure is beneficial for phase stabilization at low temperatures.

In this study, we measured the crystal structure of β-LBSO:8.0%Nd^{3+} at room temperature and −98 °C several times. All experimental results proved that β-LBSO:8.0%Nd^{3+} crystallizes in the $P3_121$ space group, indicating that the doping of 8% of the La1 site with Nd^{3+} ions stabilizes the high-temperature phase. In other words, the 2-fold rotation axis of the high-temperature phase is maintained as the temperature decreases. Single-crystal structural analysis of β-LBSO:8.0% Nd^{3+} indicates that the two oxygen atoms (O3) of the BO_4 tetrahedron are also disordered into four positions, and the regular BO_4 tetrahedron splits into two slightly distorted BO_4 tetrahedra (Figure 3g,h). However, the site occupancy factors of the two oxygen atoms (O3), 0.5 and 0.5, and the B−O bond distances, which fall into two groups of 1.396 and 1.593 Å, are different from those in the α-LBSO sample at low temperature (Figure 3d,e). Such a regular statistical distribution of the BO_4 tetrahedra has a 2-fold symmetry which is consistent with the

https://doi.org/10.1021/jacs.2c04331
J. Am. Chem. Soc. 2022, 144, 11822−11830

symmetry of the β-LBSO, as evidenced by the unit cells (Figure 3f,i). As a result, the 2-fold rotation axis in β-LBSO:8.0%Nd^{3+} is maintained as the temperature decreases as low as −98 °C. Compared with α-LBSO reported by Huang which is stabilized by an irregular local statistical distribution of the BO_4 tetrahedron, the β-LBSO:8.0%Nd^{3+} phase is stabilized by a regular statistical distribution of the BO_4 tetrahedron triggered by introducing 8% of Nd^{3+} ions. From the structural perspective, the introduction of Nd^{3+} ions to replace the La^{3+} sites may make the BO_4 tetrahedron more flexible to realize a regular statistical distribution to release the structural tension at a much wider temperature range, considering that the Nd^{3+} ion is slightly different from the La^{3+} ion in mass numbers, electronic-shell structures, atomic radii, and the crystal filed stabilization energy. As far as we know, this is the first time that the high-temperature $P3_121$ phase of β-LBSO has been found to be stabilized at low temperatures by a doping strategy.

Optical Spectroscopic Properties of the β-LBSO:8.0% Nd^{3+} Crystal. The polarized absorption spectrum of the β-LBSO:8.0%Nd^{3+} crystal is shown in Figure 4a, which displays an obvious anisotropy between π and σ polarization. The typical absorption peaks corresponding to the electronic transition from the ground state $^4I_{9/2}$ to the upper states such as $^4F_{3/2}$, $^4F_{9/2}$, $^2H_{11/2}$, $^2K_{13/2}$, $^4G_{7/2}$, $^4G_{9/2}$, $^4G_{5/2}$, $^2G_{7/2}$, $^4F_{7/2}$, $^4S_{3/2}$, $^4F_{5/2}$, and $^2H_{9/2}$ are present. There are three strong absorption bands with the peak wavelength of 579, 743, and 799 nm, which could be assigned to the electronic transition of $^4I_{9/2} \rightarrow {}^4G_{5/2} + {}^2G_{7/2}$, $^4I_{9/2} \rightarrow {}^4F_{7/2} + {}^4S_{3/2}$, and $^4I_{9/2} \rightarrow {}^4F_{5/2} + {}^2H_{9/2}$, respectively. Benefitting from the large energy gap and excellent optical transparency of the crystal in the ultraviolet range, the optical absorption of transitions from $^4I_{9/2}$ to $^2I_{13/2} + {}^4D_{7/2} + {}^2L_{17/2}$ with a peak wavelength of 326 nm emerges as shown in this figure. The absorption cross section σ_{abs}, which represents the absorption ability of the pumping light, was calculated by the formula

$$\sigma_{abs} = \frac{\alpha}{N_c} \tag{1}$$

where α is the absorption coefficient that equals the optical density divided by the thickness of the tested crystal plate shown in Figure S6c, and N_c is the actual concentration (8.61×10^{20} cm^{-3}) of Nd^{3+} in the β-LBSO:8.0%Nd^{3+} crystal. Therefore, the absorption cross-sectional values of the crystal at 579, 743, and 799 nm for σ polarization are 6.90×10^{-21}, 6.20×10^{-21}, and 6.87×10^{-21} cm^2, respectively. These results reveal that the β-LBSO:8.0%Nd^{3+} crystal has excellent optical absorption ability in the UV−vis−NIR range. Meanwhile, the strong absorption of 785−815 nm light promotes 808 nm LD as the pumping source for this crystal, which is the base of a compact laser system.

The electronic transition dynamics of Nd^{3+} was investigated based on the optical absorption spectra of the β-LBSO:8.0% Nd^{3+} crystal according to the Judd−Ofelt theory.[30] The experimental oscillator strength S_{mea} of the transitions identified from the optical absorption spectra between the excited manifold and the ground state $^4I_{9/2}$ was calculated by the following formula[31]

$$S_{exp} = \frac{3ch(2J+1)}{8\pi^3 e^2 \bar{\lambda}}\left[\frac{9n}{(n^2+2)}\right]\int \sigma(\lambda)\, d\lambda \tag{2}$$

where $\sigma(\lambda)$ is the absorption cross section, $\bar{\lambda}$ is the mean wavelength of the absorption band, J is the total angular momentum of the initial level ($J = 9/2$ for Nd^{3+}), n is the refractive index, e is the electric charge, and c is the velocity of light. According to the Judd−Ofelt theory, the experimental oscillator strength of an electric-diode transition between the initial J manifold $|(S,L),J\rangle$ and the terminal J' manifold $|(S',L')J'\rangle$ can be expressed with the three-parameter formula

$$S_{cal} = \sum_{\lambda=2,4,6} \Omega_\lambda |\langle\langle(S,L)J\|U^{(\lambda)}\|(S',L')J'\rangle|^2 \tag{3}$$

where $\langle\|U^{(\lambda)}\|\rangle$ are the doubly reduced unit tensor operators. Since the reduced matrix elements hardly vary in different hosts, the values provided by Carnall for Nd^{3+} was used to calculate the intensity parameters Ω_λ (λ = 2, 4, and 6) of the β-LBSO:8.0%Nd^{3+} crystal through a least-squares-fit between S_{cal} and S_{exp}. To justify the calculation results, we calculated the root-mean-squared deviation (RMSΔS) between the experimental and calculation line strengths, which is defined by

$$\mathrm{RMS}\Delta S = \sqrt{\frac{\sum_{i=1}^{11}(S_{mea} - S_{cal})^2}{N_{tr} - N_{par}}} \tag{4}$$

where N_{tr} is the number of transitions and N_{par} is the number of the parameter. Tables 1 and S8 display the values of the Judd−Ofelt intensity parameters and oscillator strengths. The relatively low values of RMSΔS, 5.38% for π polarization, and 4.83% for σ polarization indicate a reliable calculation result. According to the Judd−Ofelt theory, the radiative transition probability of the Nd^{3+} electronic transitions can be estimated by eq S1. Meanwhile, the luminescence branching ratio β of the radiative transitions $^4F_{3/2} \rightarrow {}^4I_{9/2}$, $^4F_{3/2} \rightarrow {}^4I_{11/2}$, $^4F_{3/2} \rightarrow {}^4I_{13/2}$, and $^4F_{3/2} \rightarrow {}^4I_{15/2}$ was predicted by eq S2. As shown in Table 2, the predicted radiative transition of Nd^{3+} is dominated by $^4F_{3/2} \rightarrow {}^4I_{9/2}$ and $^4F_{3/2} \rightarrow {}^4I_{11/2}$, with the average optical emission wavelengths of 881.1 and 1052.6 nm, respectively. Figures 4b and S9 display the optical polarized luminescence spectra of the β-LBSO:8.0%Nd^{3+} crystal. As predicted by the Judd−Ofelt theory, the profile of the luminescence spectra of the β-LBSO:8.0%Nd^{3+} crystal is dominated by the emission band corresponding to the electronic transitions from $^4F_{3/2}$ level to $^4I_{9/2}$ and $^4I_{11/2}$ levels. Besides, the emission of $^4F_{3/2} \rightarrow {}^4I_{15/2}$ transition is too weak to be detected. The optical emission cross section of this crystal was determined through

Table 1. Judd−Ofelt Intensity Parameters of the β-LBSO:8.0%Nd^{3+} Crystal

Ω_λ (10^{-20} cm^2)	π	σ	effective
Ω_2	0.2619	1.1607	0.8611
Ω_4	0.3592	2.4792	1.7725
Ω_6	0.3986	3.3904	2.3931

Table 2. Spectral Parameters of the $^4F_{3/2} \rightarrow {}^4I_{J''}$ Transition of the β-LBSO:8.0%Nd^{3+} Crystal

		π		σ	
$^4F_{3/2} \rightarrow {}^4I_{J''}$	$\bar{\lambda}$ (nm)	A (s^{-1})	β (%)	A (s^{-1})	β (%)
$^4F_{3/2} \rightarrow {}^4I_{9/2}$	881.1	124.47	41.80	900.96	38.68
$^4F_{3/2} \rightarrow {}^4I_{11/2}$	1052.6	143.16	48.08	1171.86	50.32
$^4F_{3/2} \rightarrow {}^4I_{13/2}$	1333.3	28.64	9.61	243.63	10.46
$^4F_{3/2} \rightarrow {}^4I_{15/2}$	1851.9	1.48	0.50	12.56	0.54

the Füchtbauer–Ladenburg (F–L) method and calculated by the following equation[32]

$$\sigma_{\mathrm{em}}^{i}(\lambda) = \frac{\beta(J' \rightarrow J'')3\lambda^5 I_i(\lambda)}{8\pi n^2 c\tau_{\mathrm{r}} \sum_{i=\pi,\sigma} \int \lambda I_i(\lambda)\, \mathrm{d}\lambda} \tag{5}$$

where $I(\lambda)$ is the relative luminescence intensity and τ_{r} is the radiative lifetime determined to be 1405.72 μs by eq S3. The calculated result of the emission cross-sectional pattern shows an obvious polarization with σ emission stronger than that of π emission (Figure 4b). The most intense optical emission for $^4F_{3/2} \rightarrow {}^4I_{9/2}$ transition occurs at a wavelength of 913 nm with a cross section of 1.12 × 10^{-20} cm^2. While for the $^4F_{3/2} \rightarrow {}^4I_{11/2}$ and $^4F_{3/2} \rightarrow {}^4I_{13/2}$ transitions (σ polarization), the strongest optical emitting occurs at 1068 and 1389 nm with cross sections of 2.14 × 10^{-20} and 1.12 × 10^{-20} cm^2, respectively. The most distinctive characteristic of the photoluminescence of the β-LBSO:8.0%Nd^{3+} crystal is that the optical emission of $^4F_{3/2} \rightarrow {}^4I_{11/2}$ splits into four separate peaks at 1023, 1047, 1070, and 1086 nm, with the emission intensity of the latter three being comparable. As illustrated in Figure S10, the splitting of $^4F_{3/2} \rightarrow {}^4I_{11/2}$ emission mainly arises from the electronic transitions between the Starks sublevels of $^4F_{3/2}$ and $^4I_{11/2}$ manifolds. The comparable luminescence intensity and the suitable wavelength difference between these three optical emissions at 1047, 1070, and 1086 nm are the basis for the triple-wavelength spontaneous laser output. The luminescence decay curve of the β-LBSO:8.0% Nd^{3+} crystal is shown in Figure 4c, which could be fit well by a first-order exponential decay function of $I = A_0 \exp(-t/\tau) + A_1$ with A_0 = 6259, A_1 = 63, τ = 90.18 μs, and an adjustable R square value of 0.999. The fitting result demonstrates that there is one active lattice site for Nd^{3+} ions with a luminescence lifetime of 90.18 μs for the $^4F_{3/2}$ level.

Laser Performance of the β-LBSO:8.0%Nd^{3+} Crystal. Using a β-LBSO:8.0%Nd^{3+} crystal plate with a dimension of 2 × 2 × 3 mm^3 as gain media and 808 nm LD as the pumping source, a compact laser with the simplest structure is realized and exhibited in Figure S11. In this laser, the pumping 808 nm LD worked in a chopping manner with a frequency of 10 Hz and a duty ratio of 50%. The maximum pumping power was limited to 5 W. A maximum average output power of 235 mW was achieved when the average power of the absorbed pumping laser was 2130 mW. As displayed in Figure 5, laser output occurs when the pumping power exceeds 200 mW. The average power of the output laser linearly increases with the enhancing of pumping power, exhibiting a slope efficiency of 12.1%. Figure S12 displays the laser spectra evolution with the increase of pumping power. A laser beam with a wavelength of 1047 nm comes out in the first stage. As the pumping power increases, the 1070 nm laser appears with the 1047 nm laser at the second stage. Finally, the 1092 nm laser comes out, and the system works stably in a triple-wavelength laser operating mode, as presented in Figure 5a. The laser parameters of the β-LBSO:8.0%Nd^{3+} crystal are listed in Table 3, which summarizes the current research status of triple-wavelength lasers based on the $^4F_{3/2} \rightarrow {}^4I_{11/2}$ transition of Nd^{3+} ions. The wavelength difference between laser beams is a key criterion to judge whether a triple-wavelength laser has the potential for practical application. As displayed in this table, the β-LBSO:8.0%Nd^{3+} crystal of our work has the biggest wavelength differences of 21, 24, and 45 nm, showing the most promising practical value.[13b,33,34] The maximum wavelength difference of 45 nm is even larger than the largest value of full width at half-height of $^4F_{3/2} \rightarrow {}^4I_{11/2}$ transition reported in ref 35. Furthermore, our CW triple-wavelength laser exhibits the highest slope efficiency of 12.1% and the highest output power of 235 mW under the simplest laser experimental system. These results demonstrate that the triple-wavelength laser based on the β-LBSO:8.0%Nd^{3+} crystal has the best comprehensive laser performance and practical application potential.

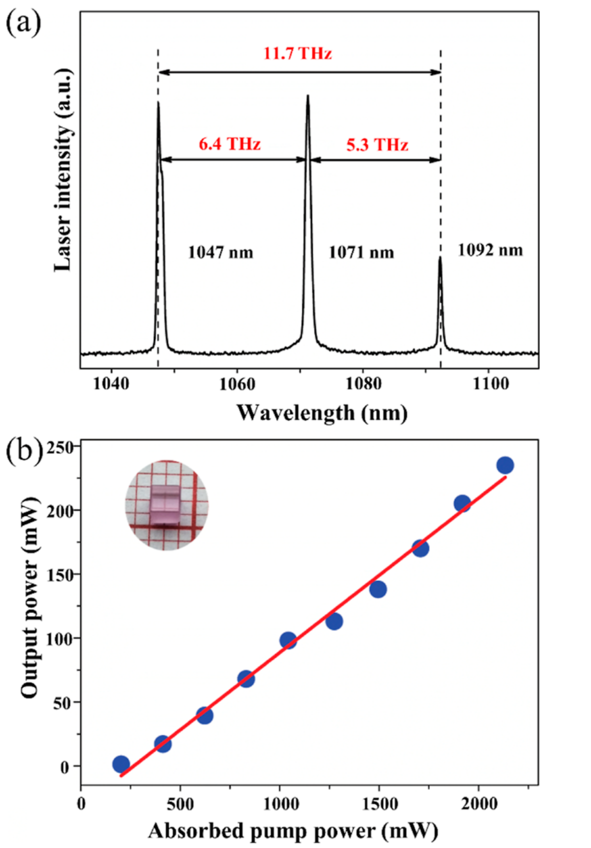

Figure 5. Laser emission spectra (a) and output power of laser emissions vs absorbed pump power (b) of the LD pumped β-LBSO:8.0%Nd^{3+} crystal laser operating at 1047, 1071, and 1092 nm.

■ CONCLUSIONS

To realize the high-performance CW triple-wavelength laser operation reported in this work, large single crystals of Nd^{3+}-doped β-LBSO were grown for the first time. The high-temperature Nd^{3+}-doped β-LBSO crystal was stabilized at room temperature by the local disorder-induced phase stabilization mechanism. When doping with more 6.3% Nd^{3+}, the BO_4 tetrahedra become statistically distributed, and the phase transition of β-LBSO is suppressed. The doping of Nd^{3+} not only eliminates the phase transition of β-LBSO but also renders the crystal optically active. The β-LBSO:8.0%Nd^{3+} crystal shows strong optical absorption in the range of 785–815 nm, which matches well with the commercial LD pumping source. The photoluminescence of the β-LBSO:8.0%Nd^{3+} crystal is dominated by the optical emission belonging to the transition of $^4F_{3/2} \rightarrow {}^4I_{9/2}$ and $^4F_{3/2} \rightarrow {}^4I_{11/2}$. In particular, the optical emission of $^4F_{3/2} \rightarrow {}^4I_{11/2}$ splits into four separate peaks at 1023, 1047, 1070, and 1086 nm. The CW triple-wavelength laser operation based on the β-LBSO:8.0%Nd^{3+} crystal was successfully achieved, with 1047, 1071, and 1092 nm lasers

https://doi.org/10.1021/jacs.2c04331
J. Am. Chem. Soc. 2022, 144, 11822−11830

Table 3. Triple-Wavelength Lasers around 1060 nm Based on the $^4F_{3/2} \rightarrow {}^4I_{11/2}$ Transition of Nd^{3+}

laser wavelengths (nm)	laser crystal	operating regime	wavelength difference (nm)	maximum output power/absorbed power, slope efficiency	refs
1076 & 1077 & 1078	SYSO:Nd3+	mode-locked pulses	1, 1, 2		33a
1059 & 1060 & 1062	YGG:Nd^{3+}	passive Q-switching	1, 2, 3		33b
1058 & 1060 & 1064	CNGG:Nd^{3+}	CW	2, 4, 6	30 mW/640 mW, 5.1%	13d
1051 & 1058 & 1061	GSGG:Cr^{3+},Nd^{3+}	CW	3, 7, 10	42 mW/4630 mW, -	34
1061 & 1065 & 1068			3, 4, 7	5 mW/4630 mW, -	
1061 & 1068 & 1072			4, 7, 11	2 mW/4630 mW, -	
1047 & 1071 & 1092	β-LBSO:8.0%Nd3+	CW	21, 24, 45	235 mW/2130 mW, 12.1%	this work

coexisting in the laser beam. The highest output power of 235 mW was obtained with a slope efficiency of 12.1%. The newly found local disorder-induced phase stabilization mechanism in our work provides a new strategy to tune the phase transition of materials. The β-LBSO:8.0%Nd^{3+} crystals obtained excel in their comprehensive triple-wavelength laser performance compared to previous reports.

■ ASSOCIATED CONTENT

Supporting Information

The Supporting Information is available free of charge at https://pubs.acs.org/doi/10.1021/jacs.2c04331.

Materials, crystal growth, characterization and Judd−Ofelt calculation, supplementary information on the crystal structure, and laser experiment; crystal structure file of β-LBSO:8.0%Nd^{3+}; and check report on the crystal structure of β-LBSO:8.0%Nd^{3+} (PDF)

Accession Codes

CCDC 2119997 contains the supplementary crystallographic data for this paper. These data can be obtained free of charge via www.ccdc.cam.ac.uk/data_request/cif, or by emailing data_request@ccdc.cam.ac.uk, or by contacting The Cambridge Crystallographic Data Centre, 12 Union Road, Cambridge CB2 1EZ, UK; fax: +44 1223 336033.

■ AUTHOR INFORMATION

Corresponding Authors

Lingyun Li − *Key Laboratory of Advanced Materials Technologies, College of Materials Science and Engineering, Fuzhou University, Fuzhou 350108, P. R. China;* orcid.org/0000-0003-0450-097X; Email: lilingyun@fzu.edu.cn

Yan Yu − *Key Laboratory of Advanced Materials Technologies, College of Materials Science and Engineering, Fuzhou University, Fuzhou 350108, P. R. China;* Email: yuyan@fzu.edu.cn

Kenneth R. Poeppelmeier − *Department of Chemistry, Northwestern University, Evanston, Illinois 60208-3113, United States;* orcid.org/0000-0003-1655-9127; Email: krp@northwestern.edu

Authors

Fazheng Huang − *Key Laboratory of Advanced Materials Technologies, College of Materials Science and Engineering, Fuzhou University, Fuzhou 350108, P. R. China*

Yi Shi − *Key Laboratory of Advanced Materials Technologies, College of Materials Science and Engineering, Fuzhou University, Fuzhou 350108, P. R. China*

Zhong-Zhen Luo − *Key Laboratory of Advanced Materials Technologies, College of Materials Science and Engineering, Fuzhou University, Fuzhou 350108, P. R. China;* orcid.org/0000-0003-4331-6286

Guo-Qiang Wang − *Key Laboratory of Advanced Materials Technologies, College of Materials Science and Engineering, Fuzhou University, Fuzhou 350108, P. R. China*

Xin-Xiong Li − *College of Chemistry, Fuzhou University, Fuzhou 350108, P. R. China;* orcid.org/0000-0002-9903-2699

Bingxuan Li − *Fujian Institute of Research on the Structure of Matter, Chinese Academy of Sciences, Fuzhou 350002, P. R. China*

Lizhen Zhang − *Fujian Institute of Research on the Structure of Matter, Chinese Academy of Sciences, Fuzhou 350002, P. R. China*

Yi Yu − *Research Center for Rare Earth Materials and Applications, School of Physics and Electronic Information, Gannan Normal University, Ganzhou 341000, P. R. China*

Ya-Nan Feng − *Key Laboratory of Advanced Materials Technologies, College of Materials Science and Engineering, Fuzhou University, Fuzhou 350108, P. R. China*

Chengkai Yang − *Key Laboratory of Advanced Materials Technologies, College of Materials Science and Engineering, Fuzhou University, Fuzhou 350108, P. R. China;* orcid.org/0000-0001-9868-4831

Complete contact information is available at: https://pubs.acs.org/10.1021/jacs.2c04331

Author Contributions

#L.L., F.H., and Y.S. contributed equally to this work.

Notes

The authors declare no competing financial interest.

■ ACKNOWLEDGMENTS

L.L., F.H., and Y.S. contributed equally to this work. The authors greatly acknowledge the support from the National Natural Science Foundation of China (nos. 51972061, U1905215, and 22109025), the National Key Research and Development Program of China (2020YFA0710303), the Natural Science Foundation of Jiangxi Province (20202ACBL214020), and the US National Science Foundation (DMR-1904701).

■ ABBREVIATIONS

LBSO $LaBSiO_5$
THz Tera Hertz
YAG yttrium aluminum garnet
YAP yttrium-aluminate
YLF lithium yttrium fluoride
CW continuous-wave
MIT metal insulator transition

LD laser diode
PXRD powder X-ray diffraction

■ REFERENCES

(1) (a) Jang, D.; Kim, K.-Y. Multicycle terahertz pulse generation by optical rectification in $LiNbO_3$, $LiTaO_3$, and BBO crystals. *Opt. Express* **2020**, *28*, 21220−21235. (b) Siegel, P. H. Terahertz technology. *IEEE Trans. Terahertz Sci. Technol.* **2002**, *50*, 910−928. (c) Zhong, K.; Yao, J.; Xu, D.; Wang, Z.; Li, Z.; Zhang, H.; Wang, P. Enhancement of terahertz wave difference frequency generation based on a compact walk-off compensated KTP OPO. *Opt. Commun.* **2010**, *283*, 3520−3524.

(2) (a) Yang, Y.; Yamagami, Y.; Yu, X.; Pitchappa, P.; Webber, J.; Zhang, B.; Fujita, M.; Nagatsuma, T.; Singh, R. Terahertz topological photonics for on-chip communication. *Nat. Photonics* **2020**, *14*, 446−451. (b) Manjappa, M.; Singh, R. Materials for terahertz optical science and technology. *Adv. Opt. Mater.* **2020**, *8*, 1901984.

(3) Petersen, E. B.; Shi, W.; Chavez-Pirson, A.; Peyghambarian, N.; Cooney, A. T. Efficient parametric terahertz generation in quasi-phase-matched GaP through cavity enhanced difference-frequency generation. *Appl. Phys. Lett.* **2011**, *98*, 121119.

(4) Ferguson, B.; Zhang, X.-C. Materials for terahertz science and technology. *Nat. Mater.* **2002**, *1*, 26−33.

(5) Taniuchi, T.; Okada, S.; Nakanishi, H. Widely tunable terahertz-wave generation in an organic crystal and its spectroscopic application. *J. Appl. Phys.* **2004**, *95*, 5984−5988.

(6) Danailov, M. B.; Milev, I. Y. Simultaneous multiwavelength operation of Nd:YAG laser. *Appl. Phys. Lett.* **1992**, *61*, 746−748.

(7) Chen, Y.-F. Cw dual-wavelength operation of a diode-end-pumped $NdYVO_4$ laser. *Appl. Phys. B: Lasers Opt.* **2000**, *70*, 475−478.

(8) Wu, B.; Jiang, P.; Yang, D.; Chen, T.; Kong, J.; Shen, Y. Compact dual-wavelength Nd:$GdVO_4$ laser working at 1063 and 1065 nm. *Opt. Express* **2009**, *17*, 6004−6009.

(9) (a) Huang, Y. J.; Chen, Y. F.; Chen, W. D.; Zhang, G. Dual-wavelength eye-safe Nd:YAP Raman laser. *Opt. Lett.* **2015**, *40*, 3560−3563. (b) Nie, W.; Cheng, C.; Jia, Y.; Romero, C.; Vázquez de Aldana, J. R.; Chen, F. Dual-wavelength waveguide lasers at 1064 and 1079 nm in Nd:YAP crystal by direct femtosecond laser writing. *Opt. Lett.* **2015**, *40*, 2437−2440.

(10) Cho, C. Y.; Huang, T. L.; Wen, S. M.; Huang, Y. J.; Huang, K. F.; Chen, Y. F. Nd:YLF laser at cryogenic temperature with orthogonally polarized simultaneous emission at 1047 nm and 1053 nm. *Opt. Express* **2014**, *22*, 25318−25323.

(11) Chen, H.; Huang, Y.; Li, B.; Liao, W.; Zhang, G.; Lin, Z. Efficient orthogonally polarized dual-wavelength Nd:$LaMgB_5O_{10}$ laser. *Opt. Lett.* **2015**, *40*, 4659−4662.

(12) Chen, Y. J.; Gong, X. H.; Lin, Y. F.; Huang, J. H.; Luo, Z. D.; Huang, Y. D. Diode-pumped orthogonally polarized dual-wavelength Nd^{3+}:$LaBO_2MoO_4$ laser. *Appl. Phys. B: Lasers Opt.* **2013**, *112*, 55−60.

(13) (a) Shayeganrad, G.; Mashhadi, L. Dual-wavelength CW diode-end-pumped a-cut Nd:YVO_4 laser at 1064.5 and 1085.5 nm. *Appl. Phys. B* **2013**, *111*, 189−194. (b) Öztürk, O. M.; Bayer, M. M.; Anwar, M. S.; Zakwan, M.; Serpengüzel, A. Spectroscopy of a Nd:YVO_4 diode pumped solid state laser. *Microw. Opt. Technol. Lett.* **2017**, *59*, 1636−1639. (c) Brenier, A.; Wu, Y.; Fu, P.; Zhang, J.; Zu, Y. Diode-pumped laser properties of Nd^{3+}-doped $La_2CaB_{10}O_{19}$ crystal including two-frequency generation with 4.6 THz separation. *Opt. Express* **2009**, *17*, 18730−18737. (d) Tan, Y.; Chen, F.; Vázquez de Aldana, J. R.; Yu, H.; Zhang, H. Tri-wavelength laser generation based on neodymium doped disordered crystal waveguide. *Opt. Express* **2013**, *21*, 22263−22268. (e) Yu, H.; Zhang, H.; Wang, Z.; Wang, J.; Yu, Y.; Shi, Z.; Zhang, X.; Jiang, M. High-power dual-wavelength laser with disordered Nd:CNGG crystal. *Opt. Lett.* **2009**, *34*, 151−153. (f) Wu, B.; Jiang, P.; Yang, D.; Chen, T.; Kong, J.; Shen, Y. Compact dual-wavelength Nd:$GdVO_4$ laser working at 1063 and 1065 nm. *Opt. Express* **2009**, *17*, 6004−6009. (g) Sun, S.; Wei, Q.; Li, B.; Shi, X.; Yuan, F.; Lou, F.; Zhang, L.; Lin, Z.; Zhong, D.; Huang, Y.; Teng, B. The $YMgB_5O_{10}$ crystal preparation and attractive multi-wavelength emission characteristics of doping Nd^{3+} ions. *J. Mater. Chem. C* **2021**, *9*, 1945−1957.

(14) Mcandrew, J.; Scott, T. R. Stillwellite, a new rare-earth mineral from queensland. *Nature* **1955**, *176*, 509−510.

(15) Belokoneva, E.; Shuvaeva, V.; Antipin, M.; Leonjuk, N. Crystal structure of a high-temperature modification of $LaBSiO_5$, a synthetic analog of stillwellite. *Zh. Neorg. Khim.* **1996**, *41*, 1097−1101.

(16) (a) Chi, L.; Chen, H.; Zhuang, H.; Huang, J. Crystal structure of $LaBSiO_5$. *J. Alloys Compd.* **1997**, *252*, L12−L15. (b) Burns, P. C.; Hawthorne, F. C.; Macdonald, D. J.; Ventura, G. D.; Parodi, G. C. The crystal structure of Stillwellite. *Can. Mineral.* **1993**, *31*, 147−152. (c) Horiuchi, N.; Uesu, Y.; Osakabe, E.; Omori, S.; Strukov, B. A. On the phase transition of new ferroelectric $LaBGeO_5$. *J. Phys. Soc. Jpn.* **1993**, *62*, 2522−2523.

(17) Leonyuk, N. I.; Belokoneva, E. L.; Bocelli, G.; Righi, L.; Shvanskii, E. V.; Henrykhson, R. V.; Kulman, N. V.; Kozhbakhteeva, D. E. High-temperature crystallization and X-ray characterization of Y_2SiO_5,Y2Si_2O_7 and $LaBSiO_5$. *J. Cryst. Growth* **1999**, *205*, 361−367.

(18) Sha, H.; Su, R.; Xiong, Z.; Wang, Z.; Shan, P.; He, C.; Yang, X.; Long, X. Borosilicate crystal $LaBSiO_5$: a new promising ultraviolet quasiphase matching material. *Adv. Opt. Mater.* **2021**, *9*, 2100080.

(19) Li, L.; Lin, Y.; Zhang, L.; Cai, Q.; Yu, Y. Flux exploration, growth, and optical spectroscopic properties of large size $LaBSiO_5$ and Eu^{3+}-substituted $LaBSiO_5$ crystals. *Cryst. Growth Des.* **2017**, *17*, 6541−6549.

(20) (a) Atkin, J. M.; Berweger, S.; Chavez, E. K.; Raschke, M. B.; Cao, J.; Fan, W.; Wu, J. Strain and temperature dependence of the insulating phases of VO_2 near the metal-insulator transition. *Phys. Rev. B: Condens. Matter Mater. Phys.* **2012**, *85*, 020101. (b) Kalcheim, Y.; Adda, C.; Salev, P.; Lee, M. H.; Ghazikhanian, N.; Vargas, N. M.; del Valle, J.; Schuller, I. K. Structural manipulation of phase transitions by self-induced strain in geometrically confined thin films. *Adv. Funct. Mater.* **2020**, *30*, 2005939. (c) You, L.; Chen, Z.; Zou, X.; Ding, H.; Chen, W.; Chen, L.; Yuan, G.; Wang, J. Characterization and manipulation of mixed phase nanodomains in highly strained $BiFeO_3$ thin films. *ACS Nano* **2012**, *6*, 5388−5394.

(21) (a) Brassard, D.; Fourmaux, S.; Jean-Jacques, M.; Kieffer, J. C.; El Khakani, M. A. Grain size effect on the semiconductor-metal phase transition characteristics of magnetron-sputtered VO_2 thin films. *Appl. Phys. Lett.* **2005**, *87*, 051910. (b) Choudhury, S.; Li, Y. L.; Krill, C., III; Chen, L. Q. Effect of grain orientation and grain size on ferroelectric domain switching and evolution: Phase field simulations. *Acta Mater.* **2007**, *55*, 1415−1426. (c) Suresh, A.; Mayo, M. J.; Porter, W. D.; Rawn, C. J. Crystallite and grain-size-dependent phase transformations in yttria-doped zirconia. *J. Am. Ceram. Soc.* **2003**, *86*, 360−362. (d) Frey, M. H.; Payne, D. A. Grain-size effect on structure and phase transformations for barium titanate. *Phys. Rev. B: Condens. Matter Mater. Phys.* **1996**, *54*, 3158−3168. (e) McKnight, R. E. A.; Moxon, T.; Buckley, A.; Taylor, P. A.; Darling, T. W.; Carpenter, M. A. Grain size dependence of elastic anomalies accompanying the alpha-beta phase transition in polycrystalline quartz. *J. Phys.: Condens. Matter* **2008**, *20*, 075229.

(22) (a) Feng, C.; Li, N.; Li, S.; Huo, Q.; Li, M.; Zhan, Q.; Li, B. H.; Yin, J.; Jiang, Y.; Yu, G. Manipulation of the magnetic exchange interaction in SmCo films with high thermal stability by controlling phase transformation. *Appl. Phys. A: Mater. Sci. Process.* **2011**, *106*, 125−129. (b) Nannuri, S. H.; Kulkarni, S. D.; K, S. C.; Chidangil, S. Post annealing induced manipulation of phase and upconversion luminescence of Cr^{3+} doped $NaYF_4$:Yb,Er crystals. *RSC Adv.* **2019**, *9*, 9364−9372.

(23) (a) Liu, W.; Lu, D.; Guo, R.; Wu, K.; Pan, S.; Hang, Y.; Sun, D.; Yu, H.; Zhang, H.; Wang, J. Broadening of the Fluorescence Spectra of Sesquioxide Crystals for Ultrafast Lasers. *Cryst. Growth Des.* **2020**, *20*, 4678−4685. (b) Zhang, L.; Wu, H.; Lin, Y.; Yuan, F.; Huang, Y.; Sun, S.; Teng, B.; Li, L.; Lin, Z. From $Sr_2Nb_2O_7$ to $Ca_xSr_{2-x}Nb_2O_7$: an effective enhancement of nonlinear optical activity by a simple way of cation substituting. *Cryst. Growth Des.* **2018**, *18*, 4140−4149. (c) Jones, R. L.; Mess, D. Improved tetragonal phase stability at

1400 °C with scandia, yttria-stabilized zirconia. *Surf. Coat. Technol.* **1996**, *86*–*87*, 94–101.
(24) (a) Saba, B.; Sarita; Varshney, P. Effect of CuO doping on the electrical behavior of ZrO_2. *Chin. J. Chem.* **2007**, *25*, 1112–1115. (b) Sobolev, A.; Musin, A.; Whyman, G.; Borodianskiy, K.; Krichevski, O.; Kalashnikov, A.; Zinigrad, M. Stabilization of cubic phase in scandium-doped zirconia nanocrystals synthesized with sol-gel method. *J. Am. Ceram. Soc.* **2018**, *102*, 3236–3243.
(25) Fan, L. L.; Chen, S.; Luo, Z. L.; Liu, Q. H.; Wu, Y. F.; Song, L.; Ji, D. X.; Wang, P.; Chu, W. S.; Gao, C.; Zou, C. W.; Wu, Z. Y. Strain dynamics of ultrathin VO_2 film grown on TiO_2 (001) and the associated phase transition modulation. *Nano Lett.* **2014**, *14*, 4036–4043.
(26) (a) Giraldi, T. R.; Dias, J. A.; Baggio, C. M.; Maestrelli, S. C.; Oliveira, J. A. Anatase-to-rutile transition in co-doped TiO_2 pigments. *J. Sol-Gel Sci. Technol.* **2017**, *83*, 115–123. (b) Nayak, S.; Sahoo, B.; Khastgir, D. Flexible nanocomposites comprised of poly-(dimethylsiloxane) and high-permittivity TiO_2 nanoparticles doped with La^{3+}/Cu^{+} for dielectric applications. *ACS Appl. Nano Mater.* **2019**, *2*, 4211–4221. (c) Priyanka, K. P.; Revathy, V. R.; Rosmin, P.; Thrivedu, B.; Elsa, K. M.; Nimmymol, J.; Balakrishna, K. M.; Varghese, T. Influence of La doping on structural and optical properties of TiO_2 nanocrystals. *Mater. Charact.* **2016**, *113*, 144–151.
(27) Luo, T.; Wan, X. J.; Jiang, Sh. X.; Zhang, L. Y.; Hong, Zh. Q.; Liu, J. Preparation and photocatalytic performance of fibrous Tb^{3+}-doped TiO_2 using collagen fiber as template. *Appl. Phys. A: Mater. Sci. Process.* **2018**, *124*, 304.
(28) (a) Nehru, L. C.; Marimuthu, K.; Jayachandran, M.; Lu, C. H.; Jagannathan, R. Ce^{3+}-doped stillwellites a new luminescent system with strong ion lattice coupling. *J. Phys. D: Appl. Phys.* **2001**, *34*, 2599–2605. (b) Wang, Z.; Cheng, P.; He, P.; Liu, Y.; Zhou, Y.; Zhou, Q. Luminescent properties and energy transfer in the green phosphors $LaBSiO_5$:Tb^{3+}, Ce^{3+}. *J. Biolumin. Chemilumin.* **2015**, *30*, 719–722. (c) Wang, Z.; Cheng, P.; Liu, Y.; Zhou, Y.; Zhou, Q.; Guo, J. Novel red phosphors $LaBSiO_5$ co-doped with Eu^{3+}, Al^{3+} for near-UV light-emitting diodes. *Opt. Mater.: X* **2014**, *37*, 277–280.
(29) (a) Juwhari, H. K.; White, W. B. Luminescence of rare earth borosilicates with the stillwellite and related structures. *Mater. Lett.* **2010**, *64*, 1751–1754. (b) Zhou, L.; Zhou, W.; Shi, R.; Liu, C.; Huang, Y.; Tao, Y.; Liang, H. Luminescence and energy transfer of Ce^{3+} and Pr^{3+} in $LaBSiO_5$. *J. Lumin.* **2016**, *177*, 178–183.
(30) (a) Judd, B. R. Optical absorption intensities of rare-earth ions. *Phys. Rev.* **1962**, *127*, 750–761. (b) Ofelt, G. S. Intensities of crystal spectra of rare-earth ions. *J. Chem. Phys.* **1962**, *37*, 511–520.
(31) (a) Chen, W.; Li, L.; Li, X.-X.; Lin, L.-D.; Wang, G.; Zhang, Z.; Li, L.; Yu, Y. Layered rare earth–organic framework as highly efficient luminescent matrix: the crystal structure, optical spectroscopy, electronic transition, and luminescent sensing properties. *Cryst. Growth Des.* **2019**, *19*, 4754–4764. (b) Li, L.; Wang, G.; Huang, Y.; Zhang, L.; Lin, Z.; Wang, G. Crystal growth and spectral properties of Nd^{3+}:$Ca_9Gd(VO_4)_7$ crystal. *J. Cryst. Growth* **2011**, *314*, 331–335.
(32) (a) Aull, B.; Jenssen, H. Vibronic interactions in Nd:YAG resulting in nonreciprocity of absorption and stimulated emission cross sections. *IEEE J. Quantum Electron.* **1982**, *18*, 925–930. (b) Yasyukevich, A. S.; Shcherbitskii, V. G.; Kisel', V. É.; Mandrik, A. V.; Kuleshov, N. V. Integral method o Reciprocity in the spectroscopy of laser crystals with impurity centers. *J. Appl. Spectrosc.* **2004**, *71*, 202–208.
(33) (a) Hou, J.; Zheng, L. H.; He, J. L.; Xu, J.; Zhang, B. T.; Wang, Z. W.; Lou, F.; Wang, R. H.; Liu, X. M. A tri-wavelength synchronous mode-locked Nd:SYSO laser with a semiconductor saturable absorber mirror. *Laser Phys. Lett.* **2014**, *11*, 035803. (b) Yu, H.; Wu, K.; Yao, B.; Zhang, H.; Wang, Z.; Wang, J.; Zhang, X.; Jiang, M. Efficient triwavelength laser with a Nd:YGG garnet crsytal. *Opt. Lett.* **2010**, *35*, 1801–1803.
(34) Demirbas, U.; Uecker, R.; Fujimoto, J. G.; Leitenstorfer, A. Multicolor lasers using birefringent filters: experimental demonstration with Cr:Nd:GSGG and Cr. *Opt. Express* **2017**, *25*, 2594–2607.
(35) Zhang, Y.; Wang, G. Spectroscopic properties of Nd:$Sr_3Gd_2(BO_3)_4$. *Phys. Status Solidi A* **2012**, *209*, 1128–1133.